Supplementary Information

Particle size determination from TEM

Reliable size determination from TEM micrographs is only possible when the hexaferrite particles are either aligned with their faces flat towards the incoming electron beam or aligned perpendicular to the grid (particles stacked on their edges). Flat-lying particles were measured edge-to-edge for their width dimensions along *{hk0}*. Meanwhile, for perpendicularly stacked particles, the thicknesses were measured along *{00l}* dimension. Particles stacked at other angles to the grid surface were not considered for size measurements. It was also understood that these criteria would still not suffice for the case of the composites where spinel and hexaferrite phases were simultaneously presented and often difficult to distinguish. For this, particle sizes of all observed particles were measured, and the size distribution histograms have been presented in Figure S6 and have been tabulated in Table 1 & Table S6 as $D_{\text{particle-\{all\}}}$. Particle size measurements for all samples were obtained for at least 150 particles, from at least 4 different micrographs in which different regions of the sample containing TEM grids were imaged.

Magnetization & recoil loop measurements

For the magnetic hysteresis measurements, demagnetization effects accounting for the sample shape and size were corrected in all datasets. Saturation magnetization (M_S) values for the samples were calculated using the law of approach to saturation. Remanent magnetization (M_R) and coercivity (H_C) values were obtained by linear positive intercepts of the demagnetization-corrected curves at H = 0 kA/m and M = 0 Am^2/kg respectively. The maximum energy product $(BH)_{max}$ was calculated by fitting an 2nd order polynomial to the *BH* vs *H* curve and obtaining its maximum value.
For recoil measurements, the pellets were immobilized in the sample holder between quartz rods using paraffin wax. Before beginning the recoil magnetization measurements, the samples were saturated with a field of *H* = +2393 kA/m (+3×10^4 Oe) and then brought back to the remanent state at *H* = 0 kA/m. Recoil loops were measured as the samples were subject to a negative applied reversal field (with a sweep rate of 3.9 kAm/s or 50 Oe/s) and then, similarly, brought back to zero field. The negative reversal field was varied from *H* = -39.7 kA/m (-5×10^2 Oe) to *H* = -795.8 kA/m (-10^4 Oe) in increments of 39.7 kA/m (5×10^2 Oe). No demagnetization corrections were performed on the obtained recoil magnetization data. The area between the demagnetizing and magnetizing parts of each recoil loop was calculated numerically. The obtained areas were then normalized to half the major hysteresis loop area. The recoil remanent magnetization (M_{recoil}) was defined as the magnetization value at zero field obtained after removal of the reversal field. Recoil remanence ratios were then calculated as M_{recoil}/M_R. [70,71,74]

Magnetic structure models

$SrFe_{12}O_{19}$ magnetic phase: 12 magnetic symmetry operations for *P*-1

```
P-1                 <--Space group symbol for hkl generation
!Nsym Cen Laue MagMat
 12   2 12   1
!
SYMM x,y,z
MSYM u,v,w, 0.000
SYMM x-y,x,z+1/2
MSYM u,v,w, 0.000
SYMM -y,x-y,z
MSYM u,v,w, 0.000
SYMM -x,-y,z+1/2
MSYM u,v,w, 0.000
SYMM -x+y,-x,z
MSYM u,v,w, 0.000
SYMM y,-x+y,z+1/2
MSYM u,v,w, 0.000
SYMM -y,-x,z
MSYM u,v,w, 0.000
SYMM -x,-x+y,z+1/2
MSYM u,v,w, 0.000
SYMM -x+y,y,z
MSYM u,v,w, 0.000
SYMM y,x,z+1/2
MSYM u,v,w, 0.000
```

SYMM x,x-y,z
MSYM u,v,w, 0.000
SYMM x-y,-y,z+1/2
MSYM u,v,w, 0.000

$Zn_{0.2}Co_{0.8}Fe_2O_4$ magnetic phase: 24 magnetic symmetry operations for *F*-1
F -1 <--Space group symbol for hkl generation
!Nsym Cen Laue MagMat
24 2 1 1
!
SYMM x,y,z
MSYM u,v,w, 0.000
SYMM -x+3/4,-y+1/4,z+1/2
MSYM u,v,w, 0.000
SYMM -x+1/4,y+1/2,-z+3/4
MSYM u,v,w, 0.000
SYMM x+1/2,-y+3/4,-z+1/4
MSYM u,v,w, 0.000
SYMM z,x,y
MSYM u,v,w, 0.000
SYMM z+1/2,-x+3/4,-y+1/4
MSYM u,v,w, 0.000
SYMM -z+3/4,-x+1/4,y+1/2
MSYM u,v,w, 0.000
SYMM -z+1/4,x+1/2,-y+3/4
MSYM u,v,w, 0.000
SYMM y,z,x
MSYM u,v,w, 0.000
SYMM -y+1/4,z+1/2,-x+3/4
MSYM u,v,w, 0.000
SYMM y+1/2,-z+3/4,-x+1/4
MSYM u,v,w, 0.000
SYMM -y+3/4,-z+1/4,x+1/2
MSYM u,v,w, 0.000
SYMM y+3/4,x+1/4,-z+1/2
MSYM u,v,w, 0.000
SYMM -y,-x,-z
MSYM u,v,w, 0.000
SYMM y+1/4,-x+1/2,z+3/4
MSYM u,v,w, 0.000
SYMM -y+1/2,x+3/4,z+1/4
MSYM u,v,w, 0.000
SYMM x+3/4,z+1/4,-y+1/2
MSYM u,v,w, 0.000
SYMM -x+1/2,z+3/4,y+1/4
MSYM u,v,w, 0.000
SYMM -x,-z,-y
MSYM u,v,w, 0.000
SYMM x+1/4,-z+1/2,y+3/4
MSYM u,v,w, 0.000
SYMM z+3/4,y+1/4,-x+1/2
MSYM u,v,w, 0.000
SYMM z+1/4,-y+1/2,x+3/4
MSYM u,v,w, 0.000
SYMM -z+1/2,y+3/4,x+1/4
MSYM u,v,w, 0.000
SYMM -z,-y,-x
MSYM u,v,w, 0.000

Additional Figures

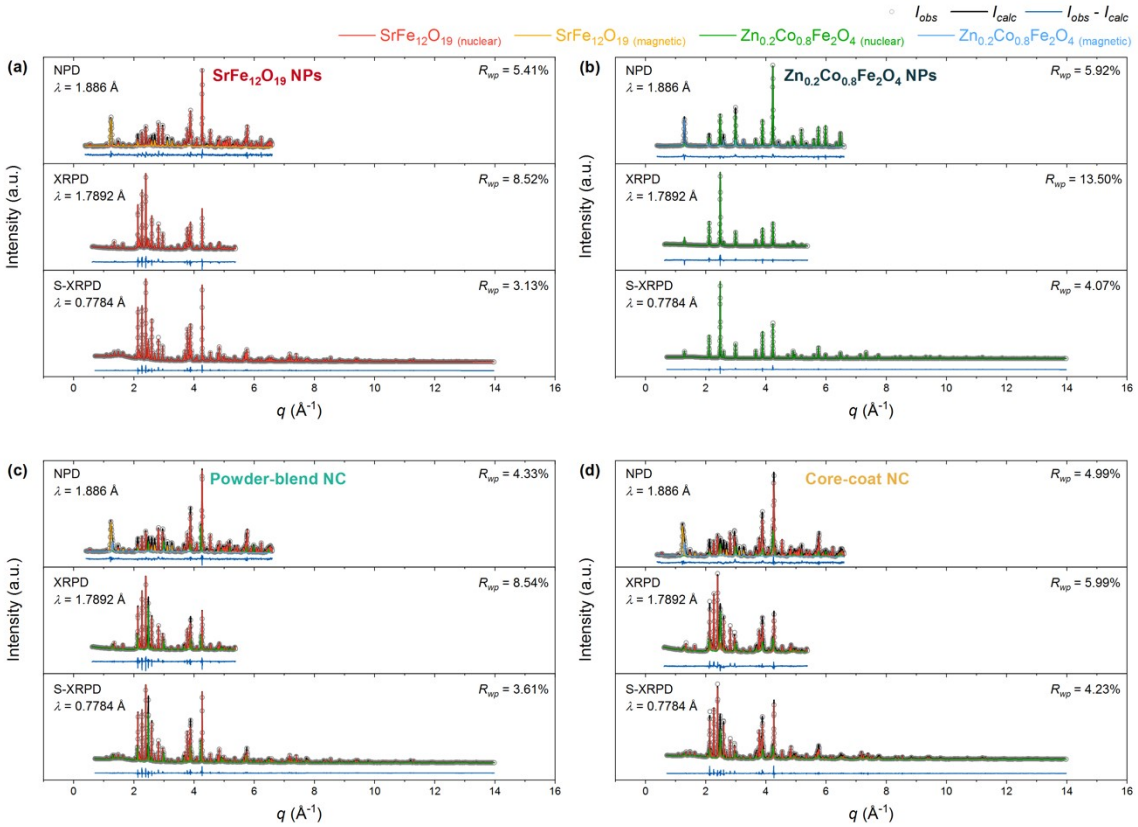

Figure S1: NPD, XRPD & S-XRPD patterns along with the corresponding combined Rietveld fits & residuals from the constrained structural models for (a) $SrFe_{12}O_{19}$ (b) $Zn_{0.2}Co_{0.8}Fe_2O_4$, (c) powder-blend NC, and (d) core-coat NC shown over the complete *q*-range for all datasets.

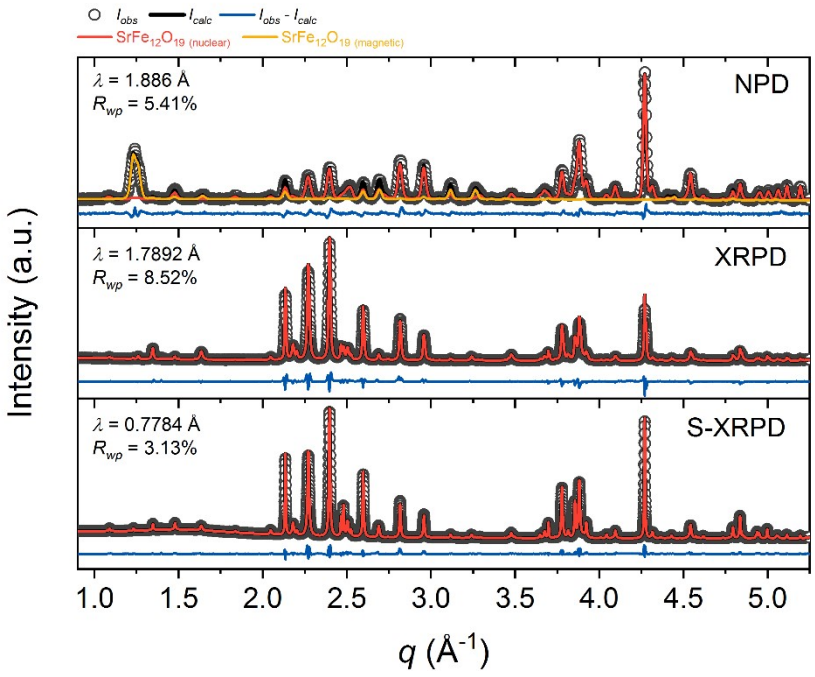

Figure S2: Detailed view (q = 0.98Å^{-1} – 5.25Å^{-1}) of NPD, XRPD & S-XRPD patterns along with the corresponding combined Rietveld fits & residuals from the constrained structural models for the $SrFe_{12}O_{19}$ NPs.

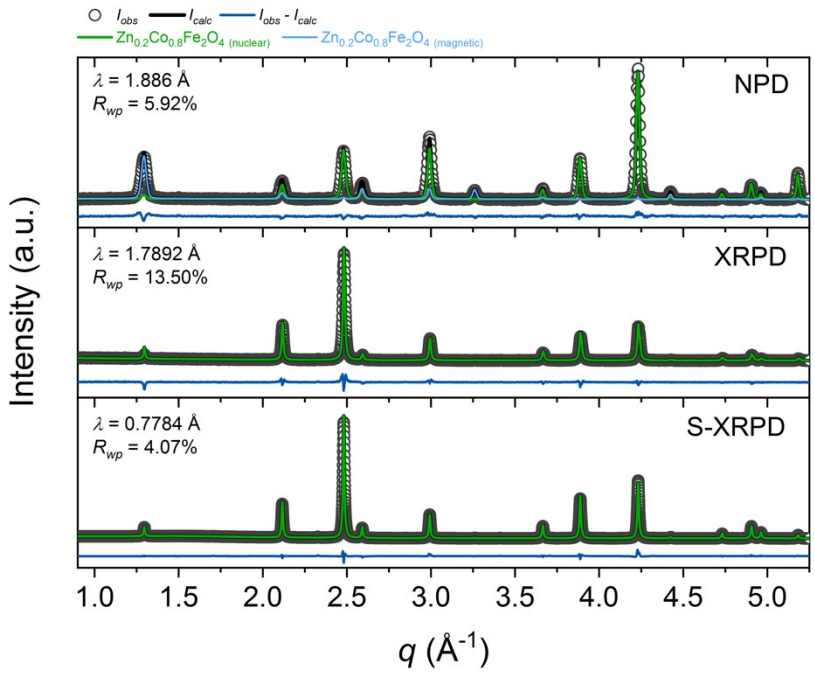

Figure S3: Detailed view (q = 0.98Å^{-1} – 5.25Å^{-1}) of NPD, XRPD & S-XRPD patterns along with the corresponding combined Rietveld fits & residuals from the constrained structural models for the $Zn_{0.2}Co_{0.8}Fe_2O_4$ NPs.

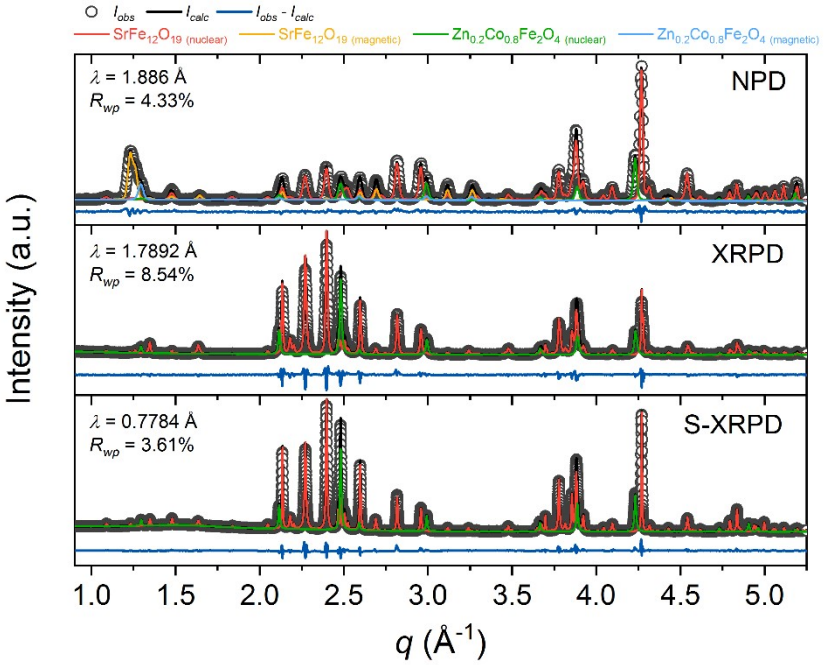

Figure S4: Detailed view (q = 0.98Å^{-1} – 5.25Å^{-1}) of NPD & XRPD patterns along with the corresponding combined Rietveld fits & residuals from the constrained structural models for the powder-blend NC.

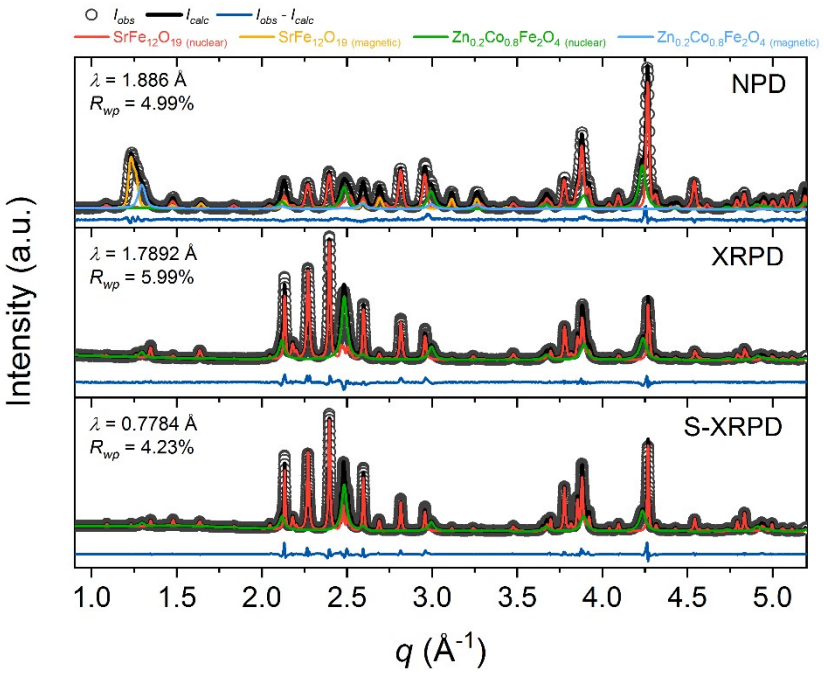

Figure S5: Detailed view (q = 0.98Å^{-1} – 5.25Å^{-1}) of NPD & XRPD patterns along with the corresponding combined Rietveld fits & residuals from the constrained structural models for the core-coat NC.

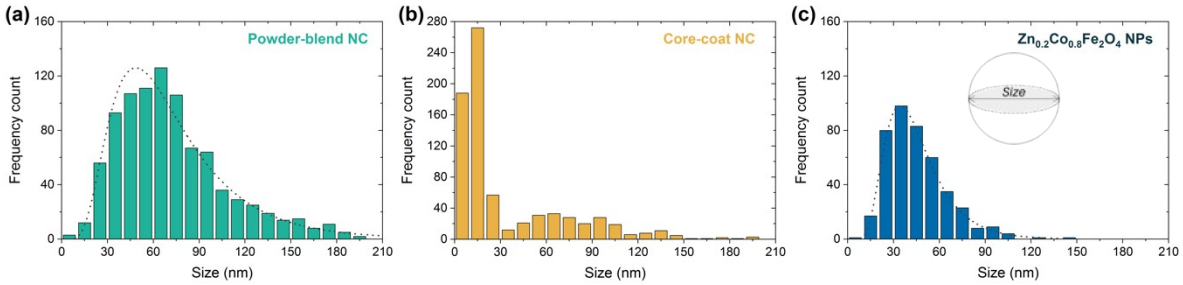

Figure S6: Histograms & log-normal fitted distribution curves of all measured crystallite sizes for the particles observed in the TEM micrographs of *(a)* powder-blend NC, *(b)* core-coat NC and *(c)* ZCFO NPs samples (bin size 10 nm)

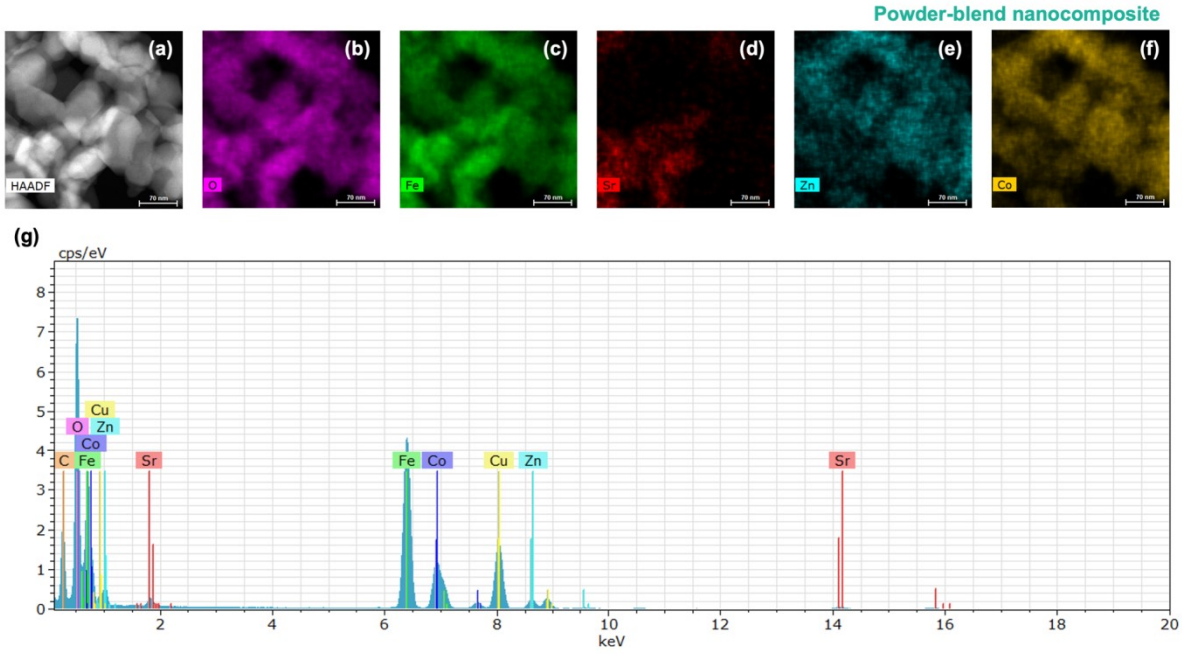

Figure S7: *(a)* STEM-HAADF micrograph of the powder-blend nanocomposite sample (shown in Figure 4) along with *(b-f)* the elemental distribution maps for O, Fe, Sr, Zn, and Co respectively in the corresponding region. *(g)* Corresponding EDX spectra with peaks matched to characteristic X-ray fluorescence lines. The fluorescence peaks for Cu and C arise from the TEM grid.

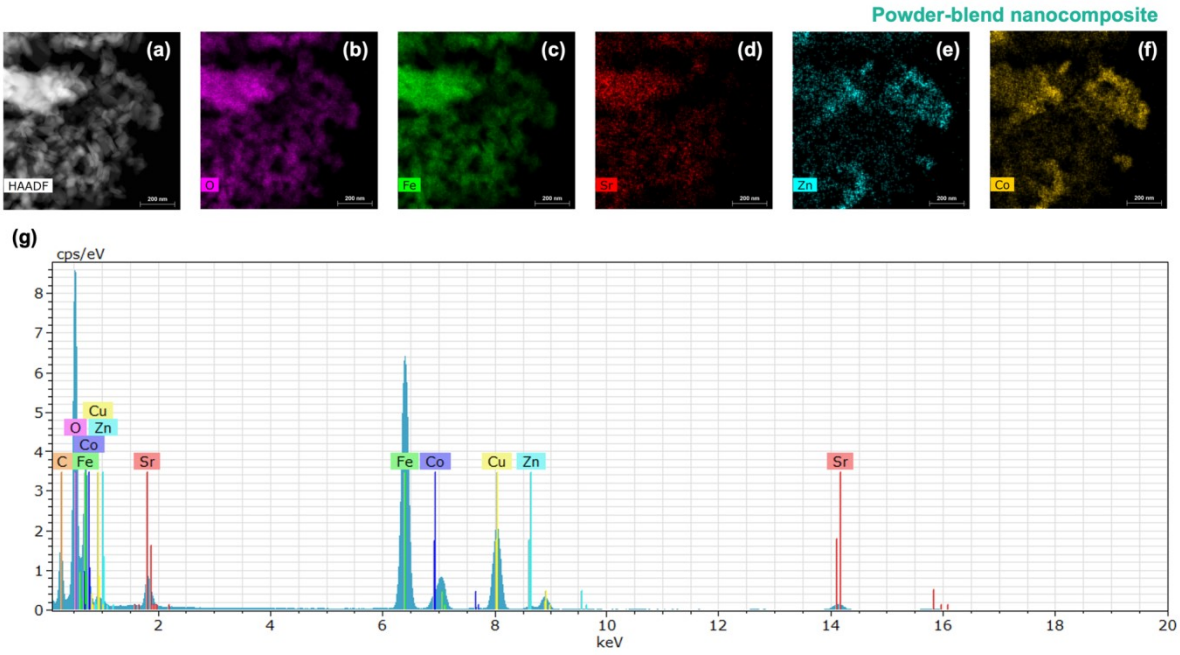

Figure S8: *(a)* STEM-HAADF micrograph of a different imaged region in the powder-blend nanocomposite sample along with *(b-f)* the elemental distribution maps for O, Fe, Sr, Zn, and Co respectively in the corresponding region. *(g)* Corresponding EDX spectra with peaks matched to characteristic X-ray fluorescence lines. The fluorescence peaks for Cu and C arise from the TEM grid.

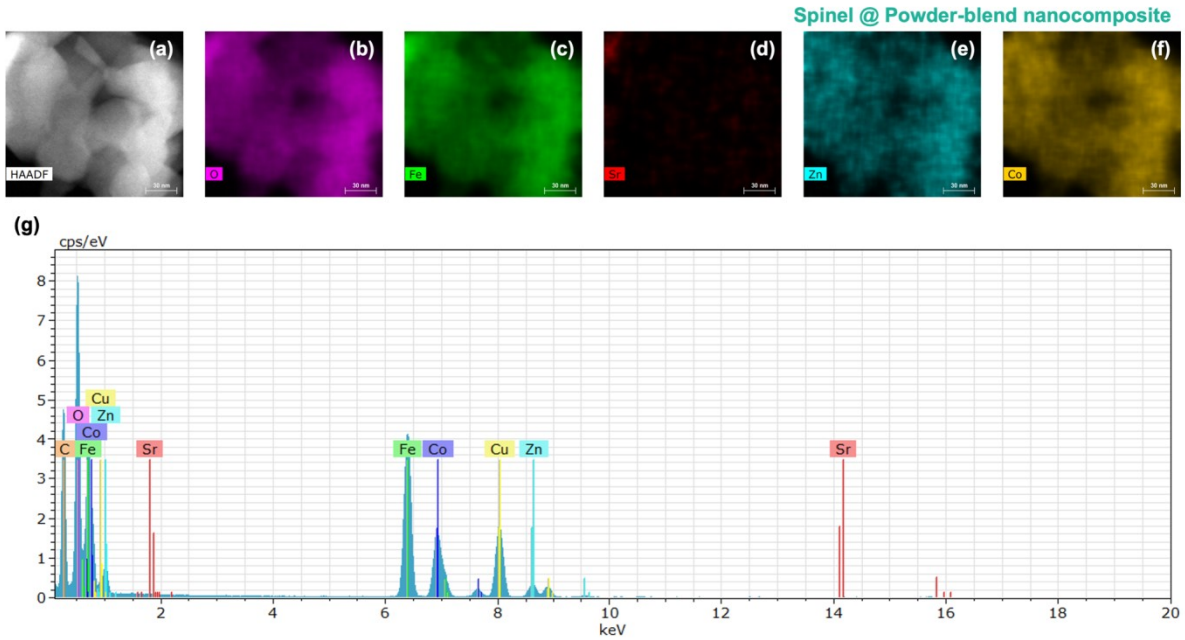

Figure S9: *(a)* STEM-HAADF micrograph of a region identified as the pure spinel phase (hexaferrite-free) in the powder-blend nanocomposite sample along with *(b-f)* the elemental distribution maps for O, Fe, Sr, Zn, and Co respectively in the corresponding region. *(g)* Corresponding EDX spectra with peaks matched to characteristic X-ray fluorescence lines. The fluorescence peaks for Cu and C arise from the TEM grid.

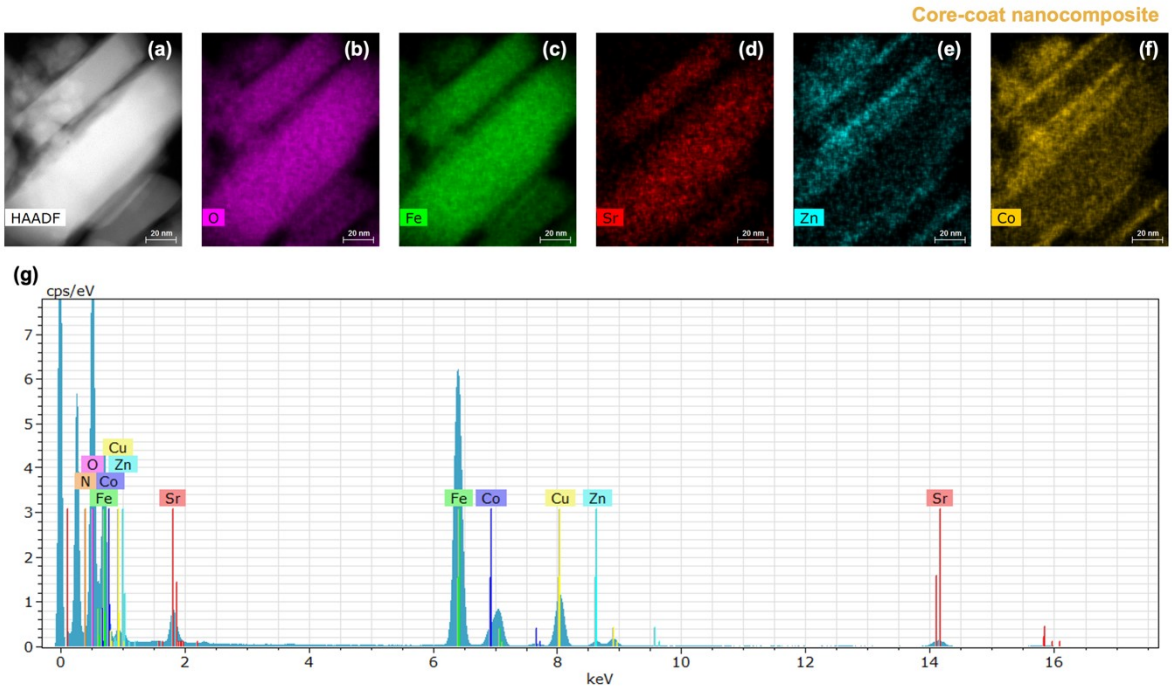

Figure S10: *(a)* STEM-HAADF micrograph of the core-coat nanocomposite (shown in Figure 4) along with *(b-f)* the elemental distribution maps for O, Fe, Sr, Zn, and Co respectively in the corresponding region. *(g)* Corresponding EDX spectra with peaks matched to characteristic X-ray fluorescence lines. The fluorescence peaks for Cu and C arise from the TEM grid.

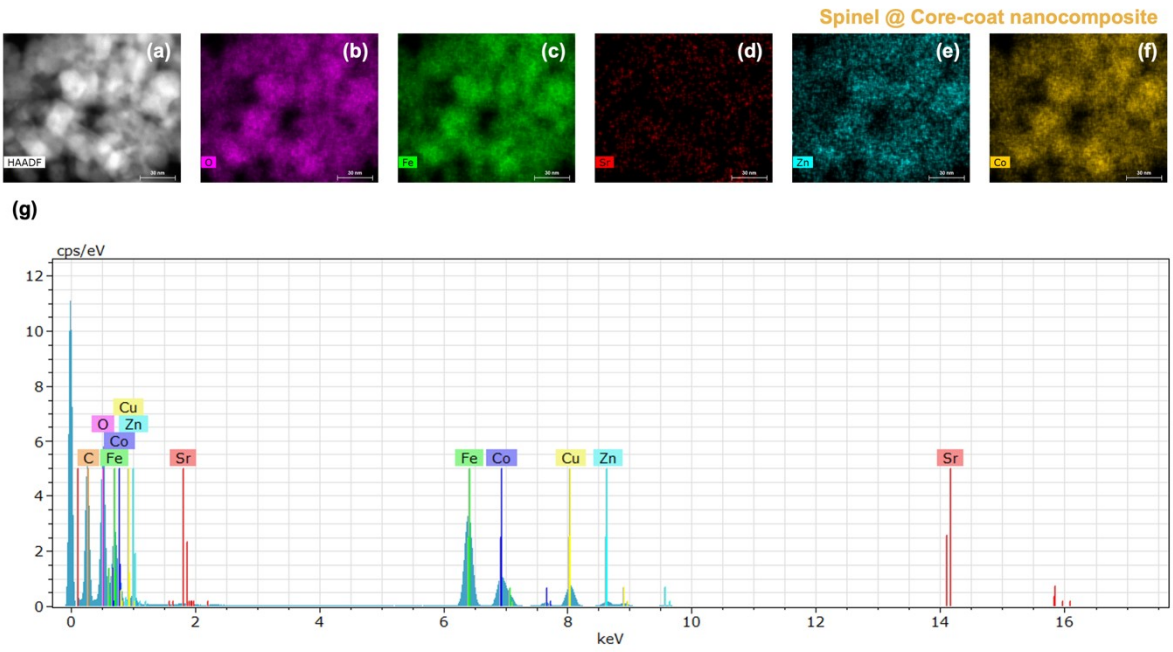

Figure S11: *(a)* STEM-HAADF micrograph of a region identified as the pure spinel phase (hexaferrite-free) in the core-coat nanocomposite sample along with *(b-f)* the elemental distribution maps for O, Fe, Sr, Zn, and Co respectively in the corresponding region. *(g)* Corresponding EDX spectra with peaks matched to characteristic X-ray fluorescence lines. The fluorescence peaks for Cu and C arise from the TEM grid.

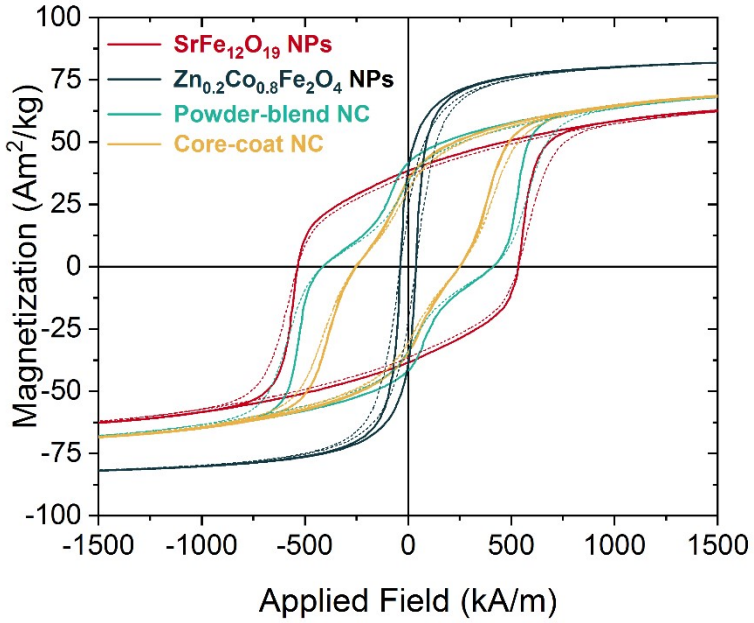

Figure S12: Comparison of M-H curves for $SrFe_{12}O_{19}$ NPs (red), $Zn_{0.2}Co_{0.8}Fe_2O_4$ NPs (indigo), powder-blend NC (teal) and core-coat NC (yellow). Dashed lines are the uncorrected curves and the solid lines have been corrected for shape demagnetization.

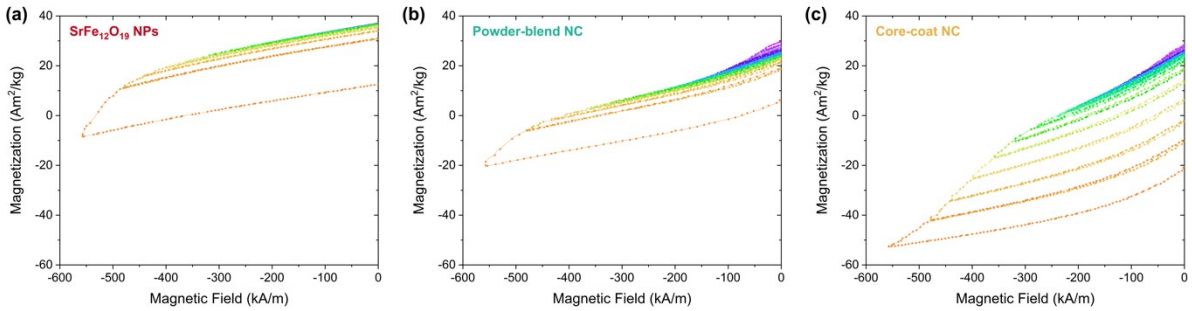

Figure S13: Recoil loops between 0kA/m and 580kA/m for (a) $SrFe_{12}O_{19}$ NPs, (b) powder-blend NC, and (c) core-coat NC. The different colors in the curves correspond to the increasing reversal fields from purple (–39.7 kA/m) to orange (–580kA/m).

Supporting Tables

Table S1: Assignment of the phases contributing to the different patterns in the combined and constrained Rietveld refinements. Structural phases contribute to both XRPD (in-house and synchrotron) and NPD patterns, while magnetic phases contribute only to the NPD patterns.

Pattern \ Phase	$SrFe_{12}O_{19}$			$Zn_{0.2}Co_{0.8}Fe_2O_4$		
	structural	magnetic @ parent	magnetic @ composite	structural	magnetic @ parent	magnetic @ composite
$SrFe_{12}O_{19}$ NPs - XRPD	x	-	-	-	-	-
$SrFe_{12}O_{19}$ NPs - NPD	x	x	-	-	-	-
$Zn_{0.2}Co_{0.8}Fe_2O_4$ - XRPD	-	-	-	x	-	-

$Zn_{0.2}Co_{0.8}Fe_2O_4$ - NPD	-	-	-	x	x	-
Powder-blend NC - XRPD	x	-	-	x	-	-
Powder-blend NC - NPD	x	-	x	x	-	x

Table S2: Consolidated summary of key refined parameters along with residual factors from the combined Rietveld analysis.

	Combined, constrained refinement									Combined refiment		
	$SrFe_{12}O_{19}$ NPs			Powder-blend NC			$Zn_{0.2}Co_{0.8}Fe_2O_4$ NPs			Core-coat NC		
	NPD	XRPD: synchrotron	XRPD: in-house	NPD	XRPD: synchrotron	XRPD: in-house	NPD	XRPD: synchrotron	XRPD: in-house	NPD	XRPD: synchrotron	XRPD: in-house
$SrFe_{12}O_{19}$ phase												
Composition & microstructure												
Wt. fraction (%)	100(7)	100.0(3)	100(3)	79(3)	77.4(2)	78(2)	-	-	-	67(3)	66.99(14)	63.9(8)
$D_{Cryst–\{hk0\}}$ (nm)	93.2(6)	93.8(6)	93.0(6)	93.6(6)	94.2(6)	93.5(6)	-	-	-	54.8(2)	54.3(2)	54.3(2)
$D_{Cryst–\{00l\}}$ (nm)	35.3(2)	35.4(2)	35.3(2)	36.6(2)	36.7(2)	36.6(2)	-	-	-	30.4(1)	30.3(1)	30.2(1)
Crystal structure												
Space group	*$P6_3/mmc$*			*$P6_3/mmc$*			-	-	-	*$P6_3/mmc$*		
Lattice *a* (Å)	5.88593(1)			5.88593(1)			-	-	-	5.88831(1)		
Lattice *c* (Å)	23.05711(5)			23.05711(5)			-	-	-	23.05268(6)		
B_{iso} Sr (Å^2)	1.007(18)			1.007(18)			-	-	-	1.202(20)		
B_{iso} Fe (Å^2)	0.3260(25)			0.3260(25)			-	-	-	0.4338(39)		
B_{iso} O (Å^2)	0.407(14)			0.407(14)			-	-	-	0.594(16)		
Magnetic structure												
Easy axis	<001>	-	-	<001>	-	-	-	-	-	<001>	-	-
μ Fe^{oct} 2a (μ_B)	4.7(2.3)	-	-	4.5(1.7)	-	-	-	-	-	4.5(1.3)	-	-
μ Fe^{oct} 12k (μ_B)	3.3(8)	-	-	3.2(7)	-	-	-	-	-	3.0(5)	-	-
μ Fe^{oct} $4f_2$ (μ_B)	– 4.4(1.0)	-	-	– 4.1(7)	-	-	-	-	-	– 4.1(6)	-	-
μ Fe^{tet} $4f_1$ (μ_B)	– 3.5(1.7)	-	-	– 3.8(1.3)	-	-	-	-	-	– 4.1(1.1)	-	-
μ Fe^{bipy} 4e (μ_B)	2.5(2.1)	-	-	3.0(1.4)	-	-	-	-	-	3.0(1.1)	-	-
M_{NPD}/unit cell (μ_B)	22(14)	-	-	22(11)	-	-	-	-	-	18(9)	-	-
Phase dependent residual factors												
R_{Bragg} (%)	4.82	6.74	6.04	3.64	4.96	4.13	-	-	-	3.52	3.26	4.36
R_F (%)	2.95	11.9	4.70	2.24	5.04	3.87	-	-	-	2.12	3.66	3.16

	Combined, constrained refinement									Combined refiment		
	$SrFe_{12}O_{19}$ NPs			Powder-blend NC			$Zn_{0.2}Co_{0.8}Fe_2O_4$ NPs			Core-coat NC		
	NPD	XRPD: synchrotron	XRPD: in-house	NPD	XRPD: synchrotron	XRPD: in-house	NPD	XRPD: synchrotron	XRPD: in-house	NPD	XRPD: synchrotron	XRPD: in-house
Magnetic R_F (%)	5.08	-	-	5.55	-	-	-	-	-	4.21	-	-
$Zn_{0.2}Co_{0.8}Fe_2O_4$ phase												
Composition & microstructure												
Wt. fraction (%)	-	-	-	21(2)	22.56(8)	22(1)	100(5)	100.0(2)	100(7)	34(2)	33.01(9)	36.1(6)
D_{Cryst} (nm)	-	-	-	49.7(6)	50.0(6)	49.6(6)	51.6(2)	52.0(3)	51.5(3)	15.7(1)	15.6(1)	15.5(1)
Crystal structure												
Space group	-	-	-	*Fd-3m*				*Fd-3m*			*Fd-3m*	
Lattice *a* (Å)	-	-	-	8.39860(2)			8.39860(2)			8.39029(3)		
O pos., *u*	-	-	-	0.24348(9)			0.24348(9)			0.24596(15)		
B_{iso} Fe/Co/Zn (Å^2)	-	-	-	0.3628(22)			0.3628(22)			0.1113(59)		
B_{iso} O (Å^2)	-	-	-	0.610(12)			0.610(12)			0.262(20)		
Site occupancy fractions												
Co^{tet} 8b	-	-	-	0.14(2)			0.14(2)			0.000(0)		
Fe^{tet} 8b	-	-	-	0.66(2)			0.66(2)			0.801(1)		
Zn^{tet} 8b	-	-	-	0.198(1)			0.198(1)			0.197(1)		
Co^{oct} 16c	-	-	-	0.66(2)			0.66(2)			0.800(1)		
Fe^{oct} 16c	-	-	-	1.34(2)			1.34(2)			1.199(1)		
Zn^{oct} 16c	-	-	-	0.000(0)			0.000(0)			0.000(0)		
O 32e	-	-	-	4.000(0)			4.000(0)			4.000(0)		
Inversion degree γ	-	-	-	0.66			0.66			0.8		
Magnetic structure												
Easy axis	-	-	-	<100>	-	-	<100>	-	-	<100>	-	-
μ Co^{tet} 8b (μ_B)	-	-	-	– 2.3(1.5)	-	-	– 2.4(5)	-	-	– 2.2(8)	-	-
μ Fe^{tet} 8b (μ_B)	-	-	-	– 3.9(2.4)	-	-	– 4.0(8)	-	-	– 3.8(1.2)	-	-
μ Co^{oct} 16c (μ_B)	-	-	-	2.4(9)	-	-	2.2(3)	-	-	2.6(6)	-	-
μ Fe^{oct} 16c (μ_B)	-	-	-	4.0(1.6)	-	-	3.7(5)	-	-	4.4(8)	-	-

	Combined, constrained refinement									Combined refiment		
	$SrFe_{12}O_{19}$ NPs			Powder-blend NC			$Zn_{0.2}Co_{0.8}Fe_2O_4$ NPs			Core-coat NC		
	NPD	XRPD: synchrotron	XRPD: in-house	NPD	XRPD: synchrotron	XRPD: in-house	NPD	XRPD: synchrotron	XRPD: in-house	NPD	XRPD: synchrotron	XRPD: in-house
Phase dependent residual factors												
R_{Bragg} (%)	-	-	-	4.09	4.18	3.18	4.11	4.81	7.85	3.14	1.82	2.86
R_F (%)	-	-	-	2.21	3.37	2.37	2.52	9.11	6.55	1.9	1.33	2.1
Magnetic R_F (%)	-	-	-	6.12	-	-	11.1	-	-	4.47	-	-
Global parameters												
Pattern dependent residual factors												
R_p (%)	4.17	2.79	6.67	3.39	3.09	6.79	4.66	3.58	9.58	3.84	3.29	4.67
Rwp (%)	5.41	3.13	8.52	4.33	3.61	8.54	5.92	4.07	13.50	4.91	4.23	5.99
Rexp (%)	3.26	0.28	3.27	2.43	0.27	3.62	3.71	0.28	9.83	2.79	0.27	3.62
$\chi^2_{pattern}$	2.76	128	6.81	3.17	185	5.57	2.54	207	1.87	3.11	253	2.74
χ^2_{global}	61.3									86.2		
Data												
Wavelength (Å)	1.8862(4)	0.77848	1.7892	1.8862(4)	0.77848	1.7892	1.8862(4)	0.77848	1.7892	1.8868(8)	0.77848	1.7892
No. of refined bkg. params.	6	17	6	6	9	6	6	9	6	6	37	6
No. of reflections	1888	1583	127	2279	1784	148	391	197	21	2279	1843	163
No. of refined params (total)	119									89		
No. of data points	3220	33519	5916	3220	33519	5916	3220	33519	5916	3220	33519	5916

Table S3: Refined values of the sitewise magnetic moments from the 'constrained magnetic moment' and 'free magnetic moment' models. Apart from the constraints on the magnetic moments, the two models were identical and both refinements led to similar values for all other refined parameters.

	Sample	$SrFe_{12}O_{19}$ NPs		Powder-blend NC		Core-coat NC	
		Constrained moments	*Free moments*	*Constrained moments*	*Free moments*	*Constrained moments*	*Free moments*
Hexaferrite	μ Fe^{oct} $2a$ (μ_B) × $2_{atoms/cell}$	3.7(2)	4.7(2.3)	3.7(2)	4.5(1.7)	3.7(1)	4.5(1.3)
	μ Fe^{oct} $12k$ (μ_B) × $12_{atoms/cell}$	3.7(2)	3.3(8)	3.7(2)	3.2(7)	3.7(1)	3.0(5)
	μ Fe^{oct} $4f_2$ (μ_B) × $4_{atoms/cell}$	–3.7(2)	–4.4(1.0)	–3.7(2)	–4.1(7)	–3.7(1)	–4.1(6)
	μ Fe^{tet} $4f_1$ (μ_B) × $4_{atoms/cell}$	–3.7(2)	–3.5(1.7)	–3.7(2)	–3.8(1.3)	–3.7(1)	–4.1(1.1)

	μ Fe^{bipy} 4*e* (μ_B) × $2_{atoms/cell}$	3.7(2)	2.5(2.1)	3.7(2)	3.0(1.4)	3.7(1)	3.0(1.1)
	M_{NPD}/unit cell (μ_B)	29(3)	22(14)	29(3)	22(11)	29(2)	18(9)

	Sample	$Zn_{0.2}Co_{0.8}Fe_2O_4$ NPs		Powder-blend NC		Core-coat NC	
		Constrained moments	*Free moments*	*Constrained moments*	*Free moments*	*Constrained moments*	*Free moments*
Spinel	μ Co^{tet} 8*b* (μ_B)	–2.3(1)	–2.4(5)	–2.4(3)	–2.3(1.5)	–2.5(2)	–2.2(8)
	μ Fe^{tet} 8*b* (μ_B	–3.8(2)	–4.0(8)	–3.9(5)	–3.9(2.4)	–4.1(3)	–3.8(1.2)
	μ Zn^{tet} 8*b* (μ_B)	0.0	0.0	0.0	0.0	0.0	0.0
	μ Co^{oct} 16*c* (μ_B)	2.3(1)	2.2(3)	–2.4(3)	2.4(9)	–2.5(2)	2.6(6)
	μ Fe^{oct} 16*c* (μ_B)	3.8(2)	3.7(5)	–3.9(5)	4.0(1.6)	–4.1(3)	4.4(8)
	μ Zn^{oct} 16*c* (μ_B)	0.0	0.0	0.0	0.0	0.0	0.0
	M_{NPD}/unit cell (μ_B)	30(3)	28(7)	31(6)	32(22)	29(3)	34(12)

Table S4: Refined fractional coorinates in the atomic structure models for the contributing hexaferrite phase.

Atom	Wyckoff positio	$SrFe_{12}O_{19}$ NPs & Powder-blend NC			Core-coat NC		
		x	*y*	*z*	*x*	*y*	*z*
Sr	2*d*	0.3333	0.6667	0.75	0.3333	0.6667	0.75
$(Fe1)^{oct}$	2*a*	0.0	0.0	0.0	0.0	0.0	0.0
$(Fe2)^{oct}$	12*k*	0.16863(12)	0.33714(23)	-0.10911(2)	0.16860(13)	0.33704(25)	-0.10919(2)
$(Fe4)^{oct}$	$4f_2$	0.33333	0.66667	0.19086(3)	0.33333	0.66667	0.19109(3)
$(Fe3)^{tet}$	$4f_1$	0.33333	0.66667	0.02724(4)	0.33333	0.66667	0.02713(4)
$(Fe5)^{bipy}$	4*e* (0.5 occ.)	0.0	0.0	0.25710(8)	0.0	0.0	0.25692(9)
O1	4*e*	0.0	0.0	0.15001(14)	0.0	0.0	0.14961(15)
O2	4*f*	0.33333	0.66667	-0.05516(15)	0.33333	0.66667	-0.05428(16)
O3	6*h*	0.18254(62)	0.3650(12)	0.25	0.18193(67)	0.3639(14)	0.25
O4	$12k_1$	0.15796(44)	0.31595(88)	0.05241(8)	0.15767(49)	0.31533(99)	0.05296(8)
O5	$12k_2$	0.50446(61)	0.0089(12)	0.15204(8)	0.50506(64)	0.0101(13)	0.15167(9)

Table S5: Stoichiometric formulas and inversion degrees for the spinel phase in the samples obtained from the combined Rietveld refinements.

Spinel in sample	Stoichiometric formula	Inversion degree γ
Powder-blend NC	$[Zn^{2+}_{0.198}Co^{2+}_{0.144}Fe^{3+}_{0.659}]^{tet}$ $[Zn^{2+}_{0.0}Co^{2+}_{0.658}Fe^{3+}_{1.343}]^{oct}$ O_4	0.66
Core-coat NC	$[Zn^{2+}_{0.197}Co^{2+}_{0.0}Fe^{3+}_{0.801}]^{tet}$ $[Zn^{2+}_{0.0}Co^{2+}_{0.800}Fe^{3+}_{1.199}]^{oct}$ O_4	0.80
ZCFO NPs	$[Zn^{2+}_{0.198}Co^{2+}_{0.144}Fe^{3+}_{0.659}]^{tet}$ $[Zn^{2+}_{0.0}Co^{2+}_{0.658}Fe^{3+}_{1.343}]^{oct}$ O_4	0.66

Table S6: Mean particle sizes ($D_{particle}$) along with standard deviations (σ) extracted from the fitted log-normal distribution curves presented in Figure S6.

Sample	Dimension	μ (nm)	σ (nm)	Bin size (nm)	$N_{measurements}$
$SrFe_{12}O_{19}$ NPs	{hk0}	80.7(1)	26.5(3)	10	128
Powder-blend NC	{hk0}	92.2(1)	36.9(3)	10	172
Core-coat NC	{hk0}	110.3(1)	33.7(3)	10	148
$SrFe_{12}O_{19}$ NPs	{00l}	33.9(1)	10.8(3)	10	168
Powder-blend NC	{00l}	34.3(1)	12.8(3)	10	176
Core-coat NC	{00l}	39.0(1)	10.8(3)	10	153
$Zn_{0.2}Co_{0.8}Fe_2O_4$ NPs	d-all	45.4(1)	20.6(3)	10	420
Powder-blend NC	d-all	73.1(1)	40.9(3)	10	868
Core-coat NC	d-all	-	-	10	739

Table S7: Elemental stoichiometric ratios normalized with respect to Fe obtained from the EDX spectra presented in Figure S7Figure S11.

Elemental stoich. w.r.t. Fe	Theoretical (1:4 mix $Zn_{0.2}Co_{0.8}Fe_2O_4$: $SrFe_{12}O_{19}$)	Composite				Theoretical $Zn_{0.2}Co_{0.8}Fe_2O_4$	Spinel	
		Powder-blend NC (Figure S7)	Powder-blend NC (Figure S8)	Core-coat NC (Figure S10)			Powder-blend NC (Figure S9)	Core-coat NC (Figure S11)
Zn	0.004	0.074	0.020	0.030		0.100	0.110	0.070
Co	0.016	0.282	0.050	0.070		0.400	0.401	0.330
Sr	0.080	0.032	0.075	0.070		-	-	-